

Supplement of Earth Syst. Dynam., 10, 569–598, 2019
<https://doi.org/10.5194/esd-10-569-2019-supplement>
© Author(s) 2019. This work is distributed under
the Creative Commons Attribution 4.0 License.



Supplement of

Arctic amplification under global warming of 1.5 and 2 °C in NorESM1-Happi

Lise S. Graff et al.

Correspondence to: Lise S. Graff (lise.s.graff@met.no)

The copyright of individual parts of the supplement might differ from the CC BY 4.0 License.

NorESM1-Happi - Climate stability and present-day characteristics

This supplement presents selected features of NorESM1-Happi compared to NorESM1-M. The modifications include a doubled horizontal resolution in the atmosphere and land model and a different tuning of the aging, and thus albedo, of snow accumulated on sea ice. An error in the aerosol scheme (Kirkevåg et al., 2013) is rectified, resulting in faster condensation of secondary gaseous matter on pre-existing particles, and reduced black carbon particles (Fig. S1). Except for Fig. S1, the tables and figures show results from standard experiments used for estimating the validity of global climate and Earth system models for CMIP5. In addition to legends, the tables and figures are commented w.r.t. the model properties.

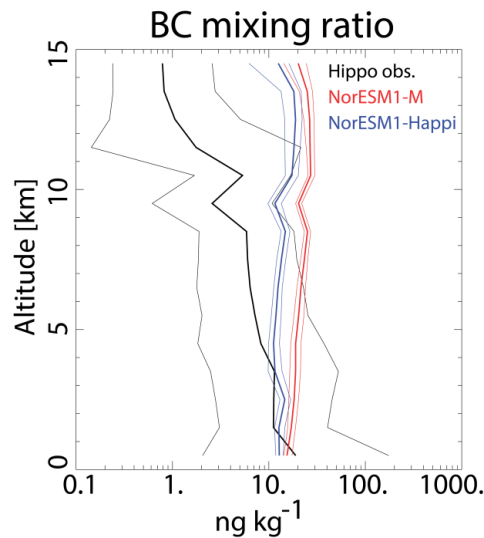


Figure S1. Vertical profiles of black carbon (BC) aerosols for present day (PD; 2006-2015) conditions estimated with NorESM1-Happi (blue) and NorESM1-M (red) using RCP8.5 (Table S1) for the same period. Thin lines indicate the calculated inter-annual range of monthly means. Black lines are mean (thick) and standard deviations (thin) of individual observations from the HIPPO campaign, with more than 700 vertical profiles during 2009–2011 from 0.3 to 14 km altitude, mainly over the Pacific Ocean between 80 °N and 67 °S (Schwartz et al., 2010 and 2013). Model-calculated monthly data are based on data sampled in the same grid-squares and for the same calendar months as the observations. Units are ng kg^{-1} .

Comments: NorESM1-M had an error in the aerosol scheme which lead to an underestimation of the turnover of BC to a hydrophilic phase. This is corrected in NorESM1-Happi, and the BC column is reduced. There is however probably still too much BC in the upper troposphere and in the stratosphere. The higher horizontal resolution in NorESM1-Happi, also influences the atmospheric aerosol burdens and residence times. The global burden of BC drops from 0.16 Tg to 0.14 Tg, primary organic matter (POM) decreases from 2.55 Tg to 2.38 Tg, and the sea-salt burden increases from 4.81 Tg to 5.21 Tg. There are negligible changes for other global aerosol burdens. Because the curves for the model data are based on monthly averages, the apparent variability is much smaller than the variability based on individually sampled observations.

Table S1. Overview of the basic model evaluation experiments for NorESM1-Happi. Details about the CMIP5 input are found at <http://cmip-pcmdi.llnl.gov/cmip5/forcing.html>.

Name	Definition	Start	Length (years)
piControl	1850 control run with constant external forcing. Greenhouse gas (GHG) concentrations follow CMIP5. The constant solar flux at the model top is 1360.9 W m^{-2} , and the constant CO_2 mixing ratio is 284.7 ppm. Aerosols and precursor emissions are from Lamarque et al. (2010); sea-salt emissions depend on surface wind and sea surface temperature (SST).	After 300 years spin-up which was started from year 600 of the NorESM1-M spin-up (Bentsen et al., 2013). First year is year 900.	500
Hist1, Hist2, Hist3	Three ensemble members for the period 1850–2015. Input: 1850–2005 solar radiation (Lean et al., 2005; Wang et al., 2005); volcanic stratospheric sulphate (Ammann et al., 2003); anthropogenic GHG conc., aerosol emissions, and land-cover from CMIP5; extension for 2006–2015 uses RCP8.5.	Branched off from piControl in years 930 (Hist1), 960 (Hist2) and 990 (Hist3).	166 (each)
GHG only	Hist1 with external forcing as in 1850, except: GHGs vary.	As for Hist1	166
Aerosol only	Hist1 with external forcing as in 1850, except: aerosols and precursor emissions vary.	As for Hist1	166
Natural only	Hist1 with external forcing as in 1850, except: natural solar radiation and volcanoes vary.	As for Hist1	166
RCP2.6, RCP4.5, RCP8.5	Future projection runs based on representative concentration pathway (RCP) scenarios according to van Vuuren et al. (2011).	Prolongation of Hist1 from 2006 until 2100.	95
abrupt $4\times\text{CO}_2$	Abrupt quadrupling of atmospheric CO_2 concentrations; to estimate Equilibrium Climate Sensitivity (ECS) and feedbacks.	Year 930 in piControl	150
gradual $4\times\text{CO}_2$	1 % increase per year of atmospheric CO_2 until quadrupling and then constant, to estimate Transient Climate Response (TCR)	Year 930 in piControl	150

Table S2. Global and annual means from the Hist1 experiment (1976–2005) performed with NorESM1-Happi and NorESM1-M and values from re-analysis data or observations (references below the table). The NorESM values are adjusted to compensate for the slight deviation between the top of the model atmosphere (abbreviated to TOA) and the top of the atmosphere as seen from satellites (Collins et al., 2006; TOA_{SAT} in this table).

Variable (unit)	NorESM1-Happi 1 ° resolution	NorESM1-M 2 ° resolution	OBS / reanalysis
TOA _{SAT} net SW flux (W m ⁻²)	240.2	234.9	240.6 ^a 244.7 ^b 234.0 ^c
TOA _{SAT} net clear-sky SW flux (W m ⁻²)	289.4	289.5	287.6 ^a 294.7 ^b 289.3 ^c
TOA _{SAT} upward LW flux (W m ⁻²)	237.6	232.4	239.6 ^a 239.0 ^b 233.9 ^c
TOA _{SAT} clear-sky upward LW flux (W m ⁻²)	263.5	262.3	266.1 ^a 266.9 ^b 264.4 ^c
TOA _{SAT} LW cloud forcing (W m ⁻²)	25.81	29.90	26.48 ^a 27.19 ^b 30.36 ^c
TOA _{SAT} SW cloud forcing (W m ⁻²)	-49.20	-54.57	-47.07 ^a -48.59 ^b -54.16 ^c
Cloud cover (%)	46.36	53.76	66.80 ^d 66.82 ^e
Cloud liquid water path (g m ⁻²)	121.3	125.3	112.6 ^f
Surface sensible heat flux (W m ⁻²)	18.0	17.8	19.4 ^h 15.8 ⁱ 13.2 ^j
Surface latent heat flux (W m ⁻²)	83.7	81.7	87.9 ^h 84.9 ^k 82.4 ^g 89.1 ^l
^a CERES-EBAF (Loeb et al., 2005, 2009, 2012); ^b CERES (Loeb et al., 2005, 2009,2012), ^c ERBE (Harrison et al., 1990; Kiehl and Trenberth, 1997), ^d ISCCP (Rossow and Schiffer, 1999; Rossow and Dueñas, 2004), ^e CLOUDSAT (L’Ecuyer et al., 2008), ^f MODIS (Greenwald, 2009; Seethala and Horváth, 2010), ^g ERA40 (Uppala et al., 2005), ^h JRA25 (Onogi et al., 2007), ⁱ NCEP (Kanamitsu et al., 2002), ^j LARYA (Large and Yeager, 2004, 2008), ^k ECMWF (Trenberth et al., 2011), ^l WHOI (Yu and Weller, 2007; Yu et al., 2008).			

Comments: The TOA_{SAT} net downward radiative flux for Hist1 is +0.61 W m⁻² in NorESM1-Happi and +0.54 W m⁻² in NorESM1-M. The cloud cover, the liquid water path, and the long- and short-wave cloud forcing in NorESM1-Happi are all smaller than in NorESM1-M. Therefore, more solar radiation is absorbed in the earth system, causing increased surface evaporation (latent heat) and increased TOA outgoing LW radiation. More than 20 % of this increase is from the clear sky conditions.

Table S3. Global means and trends of selected climate variables in the piControl experiments (500 years) with NorESM1-Happi and NorESM1-M. Linear trends are estimated by linear regression of annual averages, and their statistical significance are determined by a t-test using estimated degrees of freedom that account for autocorrelation of the data (Bretherton et al., 1999). Significant trends ($p < 0.05$) are shown in bold.

	Top of model (TOA) net radiation (W m^{-2})		Net heat-flux into the ocean (W m^{-2})		Global ocean temperature ($^{\circ}\text{C}$)	
Model	Mean	trend	mean	trend	Mean	trend
NorESM1-Happi	-0.042	+0.001	+0.004	+0.004	3.78	+0.008
NorESM1-M	+0.043	n.c.	+0.122	-0.019	3.81	+0.126
	Global ocean Salinity (g kg^{-1})		Sea-surface salinity (SSS) (g kg^{-1})		Max AMOC volume flux at 26.5°N (Sv)	
Model	Mean	trend	mean	trend	mean	trend
NorESM1-Happi	34.72	$-3.20 \cdot 10^{-4}$	34.57	+0.005	32.4	+1.0
NorESM1-M	34.72	$-3.14 \cdot 10^{-4}$	34.49	n.c.	30.8	-0.6
	Drake Passage ocean volume flux (Sv)		Near surface air temperature ($^{\circ}\text{C}$)		Sea-surface temperature (SST) ($^{\circ}\text{C}$)	
Model	Mean	trend	mean	trend	mean	trend
NorESM1-Happi	135	-6.98	12.74	-0.032	17.37	-0.021
NorESM1-M	130	-6.29	13.15	+0.037	17.68	+0.031

Comments: The imbalance at the TOA causes a small sustained cooling of the Earth system in NorESM1-Happi, as opposed to a warming in NorESM1-M (note: the value for the imbalance at TOA given in Bentsen et al. (2013) and Iversen et al. (2013) has been corrected). The small, non-zero net heat flux into the ocean causes the global-mean ocean temperature to increase, probably due to a strong AMOC. The trend in NorESM1-Happi is smaller than in NorESM1-M because the piControl from the Happi-version starts from a state closer to equilibrium. The cooling ground surface follows from the negative net TOA and positive net (downward) ocean heat fluxes. We find a statistically significant freshening of the oceans, even though the global-mean sea-surface salinity (SSS) has a positive trend. The trends in AMOC and the Drake Passage transport are comparable to those in NorESM1-M.

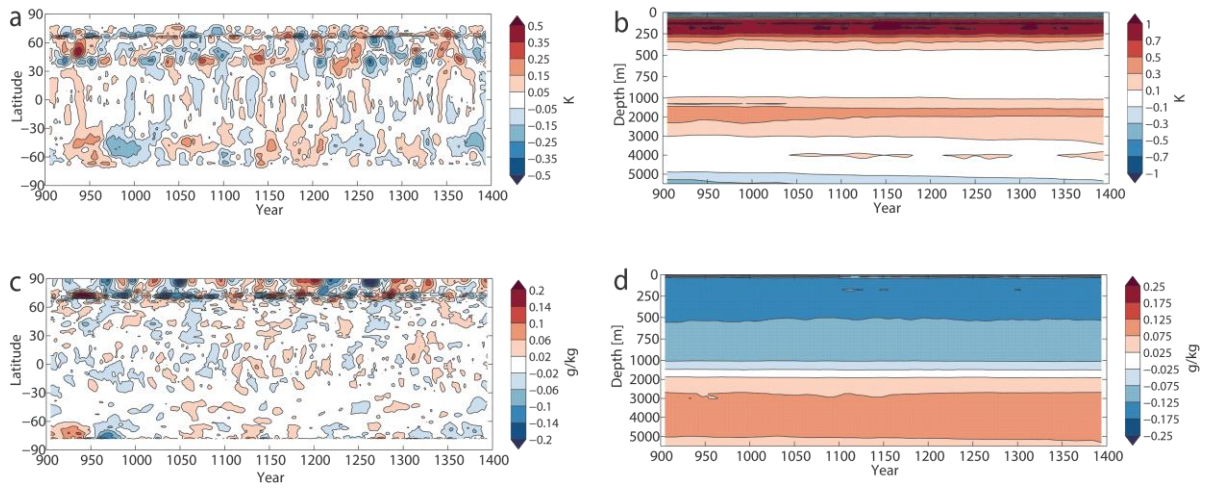


Figure S2. Latitude–time Hovmöller diagrams for the piControl experiment (900–1400) with NorESM1-Happi, showing deviations in annual-mean, zonal-mean sea-surface temperature (SST; a) and sea-surface salinity (SSS; c), where the time mean has been subtracted, and depth-time Hovmöller diagrams of deviations in annual-mean, global-mean ocean potential temperature (b) and salinity (d), where the annual-mean potential temperature and salinity of the World Ocean Atlas 2009 (Locarnini et al., 2010; Antonov et al., 2010) has been subtracted. The time series have been filtered with a 10-year running mean. Note the non-linear depth co-ordinate in (b) and (d). Units are K (a–b) and g kg^{-1} (c–d).

Comments: Except for the sea-surface values (SSS), the salinity is probably underestimated in the upper ocean layers and overestimated below. There is no clear trend, as opposed to the results for NorESM1-M (Fig. 3 in Bentsen et al., 2013), because piControl with NorESM1-Happi starts from a state closer to equilibrium. The piControl with NorESM1-Happi is more stable and deviates less from the World Ocean Atlas of 2009 than NorESM1-M (Fig. 3 in Bentsen et al., 2013).

Table S4. Bias and root-mean-square error (RMSE) for selected atmospheric variables in the Hist1 experiment (1976–2005) from NorESM1-M and NorESM1-Happi. Observational data: Cloudsat (L’Ecuyer et al., 2008); CRU (Mitchell and Jones, 2005; Morice et al., 2012); HadISST (Hurrell et al., 2008); GPCP, (Adler et al., 2003; Huffman et al., 2009); ISCCP (Rossow and Schiffer, 1999; Rossow and Dueñas, 2004). The values in the table have been produced with the diagnostic package from NCAR.

		Total cloud cover fraction (%)		T _{2m} continents CRU (K)	SST HadISST (K)	Total Precip. GPCP (mm d ⁻¹)
		Cloudsat	ISCCP			
Happi	bias	-20.46	-20.44	-1.45	-0.56	0.19
	rmse	22.08	23.01	2.40	1.19	1.15
M	bias	-13.06	-13.04	-0.88	-0.25	0.13
	rmse	15.64	17.40	2.38	1.24	1.22

Comments: The negative continental temperature bias is 0.52 K (65 %) larger and the negative sea-surface temperature (SST) bias is 0.31 K (124 %) larger in NorESM1-Happi than NorESM1-M. The cloud cover is underestimated in both model versions, and is about 7 % cloud cover fraction units smaller in NorESM1-Happi, partly due to higher horizontal resolution (as discussed by Gent et al., 2011). The ground surface in NorESM1-Happi loses more heat, while the increased short-wave radiation at the ground surface increases the evaporation and thus the surface latent heat flux increases by 2 W m⁻² (Table S2). The overestimated global-mean precipitation rate is consequently 0.06 mm d⁻¹ larger in NorESM1-Happi and is largest in the tropics (Fig. S3c and d).

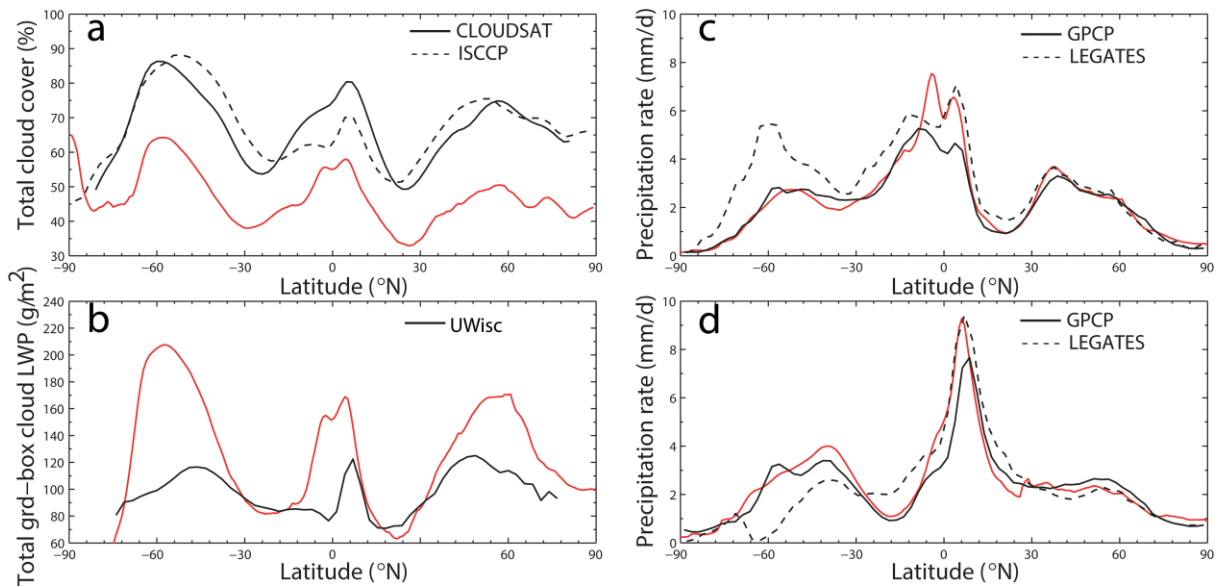


Figure S3. Zonal-mean total cloud fraction (a), total liquid water path over oceans (b) and precipitation rate (c and d) for boreal winter (December-February; DJF) and summer (June-August; JJA) for the Hist1 experiment (1976–2005) with NorESM1-Happi (red) and observations (black). Observations of cloud cover (a) are from the ISCCP D2-retrievals for the period 1983–2001 (Rossow and Schiffer, 1999; Rossow and Dueñas, 2004; black dashed curve), CLOUDSAT radar and LIDAR retrievals from September 2006–December 2010 (L’Ecuyer et al., 2008; black solid curve). Observations of liquid water path (b) are from the UWisc retrievals over oceans for the period 1988–2008 (O’Dell et al., 2008; black solid curve). Observations of precipitation (c) are from GPCP data (Adler et al., 2003; black solid curve) and Legates (Spencer, 1993; Legates and Willmott, 1990; black dashed curve). Units are % (a), g m^{-2} (b), and mm d^{-1} (c–d).

Comments: The zonal-mean cloud bias is negative at all latitudes, except close to the South Pole. The liquid water content is overestimated except in the sub-tropics (b; only values over ocean are shown). The overestimate is most pronounced over the marine extratropical cyclone regions as discussed by Jiang et al. (2012). The zonal-mean precipitation rate for winter and summer are in good agreement with the Legates data in the tropics and with the GPCP elsewhere. The overestimates in Table S4 seem to originate in the tropics.

Table S5. Monthly-mean Northern Hemisphere (NH) and Southern Hemisphere (SH) sea-ice extent and standard deviation (std) calculated for March and September from the Hist1 experiments (1979–2005) with NorESM1-Happi and NorESM1-M, and from observations (OSI-SAF, 2017). The best-estimate ice concentration fields from observations were interpolated to the model grid before the extents were calculated. Units are 10^6 km^2 .

			Extent (10^6 km^2)	Std (10^6 km^2)	Bias (10^6 km^2)
NH	March	OBS	15.41	0.42	
		M	14.34	0.25	-1.07
		Happi	14.72	0.26	-0.69
	Sept.	OBS	6.90	0.62	
		M	8.49	0.4	1.59
		Happi	7.95	0.40	1.05
SH	March	OBS	4.46	0.41	
		M	5.65	0.46	1.19
		Happi	5.17	0.51	0.71
	Sept.	OBS	18.76	0.34	
		M	19.25	0.50	0.49
		Happi	19.98	0.44	1.22

Comments: The biases in sea-ice extent are smaller in NorESM1-Happi than in NorESM1-M, except for in the SH during September. The standard deviations for the models are smaller than or equal to their biases; the simulated inter-annual variability is underestimated in the NH and slightly overestimated in the SH. The models generally overestimate the extent for the NH March maximum, although the sea-ice cover is underestimated in some areas like the Labrador Sea (Fig. S4).

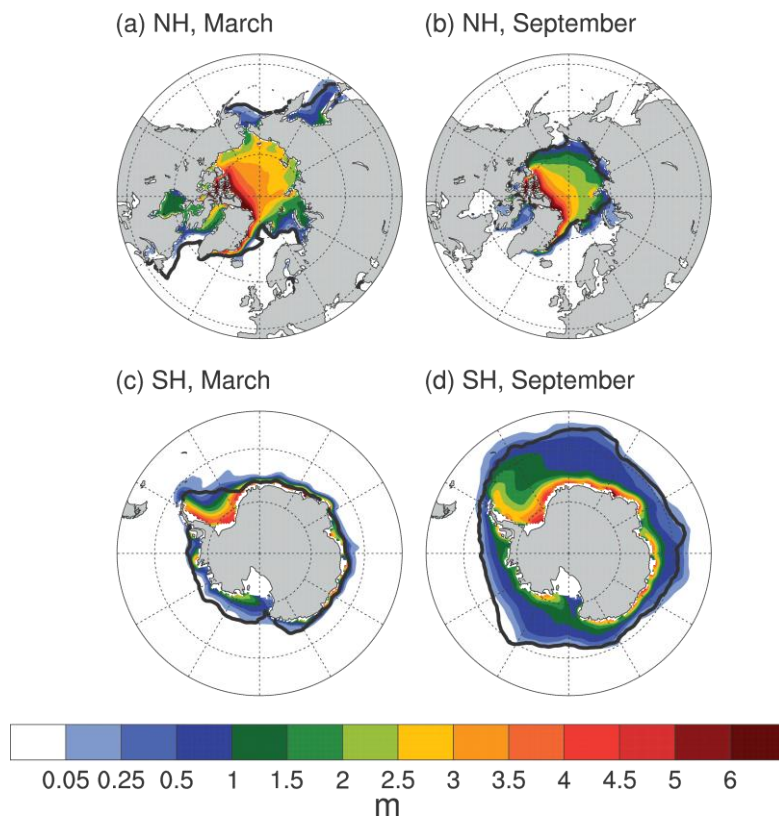


Figure S4. Mean sea-ice thickness in the Hist1 experiment (1976–2005) from NorESM1-Happi for NH March (a), NH September (b), SH March (c), and SH September (d). The solid black line shows the climatological 15 % concentration line for the same period from the OSI-SAF reprocessed data set (OSI-SAF, 2017). Units are m (a-d).

Comments: The distribution of the Arctic sea-ice thickness is considerably improved in NorESM1-Happi compared to NorESM1-M, with a pronounced cross-polar gradient with maximum thickness on the Greenland-Canadian side (around 5 m) and a minimum along the Siberian coast. This improvement was already noticed in Seland and Debernard (2014).

Table S6. Simulated changes in selected annual-mean, global-mean fields between the three RCPs (2071–2100) and the Hist1 experiment (1976–2005) from NorESM1-Happi (columns 1 to 3). Also shown is the annual-mean, global-mean values from Hist1 (column 4) and the difference between Hist1 and the 1850 piControl (column 5) from NorESM1-Happi. For comparison with the Hist1 values (column 4), we show observationally-based values for the water cycle (Trenberth et al., 2011; column 6), and values from the Hist1 experiment with NorESM1-M (Table 5 in Iversen et al., 2013; column 7).

	RCP8.5 – Hist1	RCP4.5 – Hist1	RCP2.6 – Hist1	Hist1 NorESM1- Happi	Hist1 – piControl	Water Budget 2001-2008	Hist1 NorESM1- M
T_{2m} (K)	+3.09	+1.59	+0.91	286.44	+0.55	-	286.78
SST (K)	+2.02	+1.03	+0.59	290.88	+0.36	-	282.92
$AREA_{SEAICE}$ (10^6 km^2)	-6.6	-2.8	-1.7	20.7	-1.0	-	20.76
P_{GLOBAL} $1000 \text{ km}^3 \text{ yr}^{-1}$	+28.1	+17.5	+11.9	533.5	+1.5	500	521
E_{OCEANS} $1000 \text{ km}^3 \text{ yr}^{-1}$	+26.1	+15.1	+10.1	451.7	+1.3	426	442
$(E-P)_{OCEANS}$ $1000 \text{ km}^3 \text{ yr}^{-1}$	+7.5	+3.3	+1.2	45.2	+0.6	40	43
P_{OCEANS} $1000 \text{ km}^3 \text{ yr}^{-1}$	+18.2	+11.8	+8.9	406.5	+0.7	386	399
P_{LAND} $1000 \text{ km}^3 \text{ yr}^{-1}$	+9.9	+5.7	+3.0	127.0	+0.8	114	122
E_{LAND} $1000 \text{ km}^3 \text{ yr}^{-1}$	+2.5	+2.4	+1.8	81.8	+0.2	74	79

Comments: For the period of interest, NorESM1-Happi (column 4) shows more evaporation from oceans than NorESM1-M (column 7) by approximately 10 more units ($1 \text{ unit} = 10^3 \text{ km}^3 \text{ yr}^{-1}$) of water vapour, but only approximately 2 of these units contribute to increased net transport of water vapour from oceans to continents. In addition, net evaporation from land is enhanced by 3 units, and precipitation over land is enhanced by 5 units in NorESM1-Happi. The water cycle is too fast in the model, which also shows up as a positive precipitation bias (Table S4), and possibly an increased thermohaline forcing of the Atlantic meridional overturning circulation (AMOC; Table S3 and Fig. S7).

In RCP2.6, the model produces a 1.46 K higher global temperature by 2100 than in 1850. Compared to the end of the 20th century, the simulated annual global sea-ice extent is 8.2 % smaller, global precipitation is 2.2 % larger, continental precipitation 2.4 % is larger, and continental (P-E) is 2.7 % larger. In RCP4.5, the model simulates a 2.14 K warmer world by 2100, and applying a factor 0.93 to the changes approximates a 2.0 K warmer world. In the resulting climate, the annual global-mean sea-ice extent is 12.6 % smaller, global precipitation is 3.1 % larger, continental precipitation is 4.2 % larger, and continental (P-E) is 6.8 % larger. In RCP8.5, the model indicates a 3.7 K warmer world compared to the piControl and considerably larger impacts on sea ice and the water cycle.

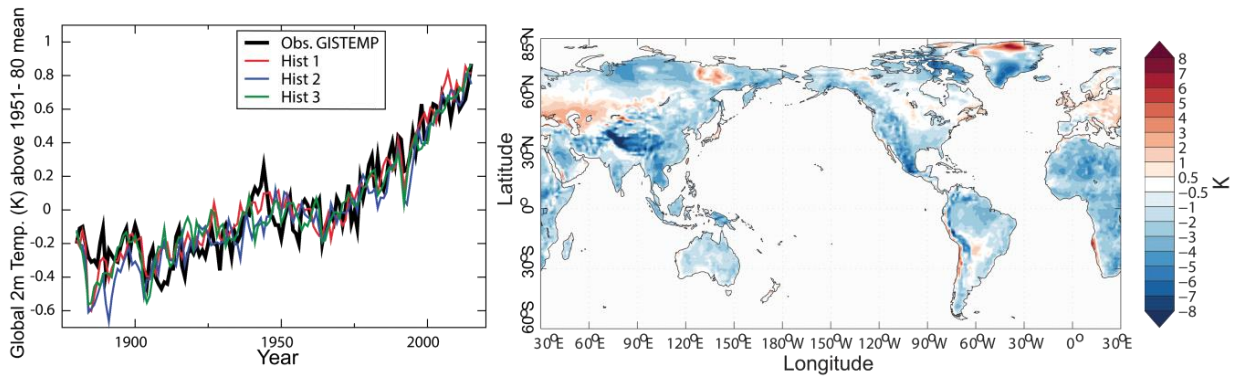


Figure S5. Time evolution of deviations of annual-mean near-surface temperature in the three historical experiments (Hist1, Hist2, and Hist3; red, blue, and green) from NorESM1-Happi and the NASA GISS global temperature record (Hansen et al., 2010; black) for the historical period (1850–2015) relative to the 1951–1980 average (left) and the difference between the near-surface temperature over land between the Hist1 experiment from NorESM1-Happi and the CRU TS3.1 (Mitchell and Jones, 2005) observational data for the period 1976–2005 (right). The global bias is -1.45 K with a RMSE of 2.40 K (compared to -0.88 K and 2.38 K for NorESM1-M, see Table S4). The colour bar on the right has a non-linear scale. Units are K (a–b).

Comments: Although the model slightly underestimates the maximum in the global temperature anomaly around 1950, there is good agreement after 1950. The temperature bias is removed in the left panel, but is evident in the right panel for the continents and in Table S4. Except for in Europe and parts of western Asia, there is a widespread underestimate, hence the global cold model bias.

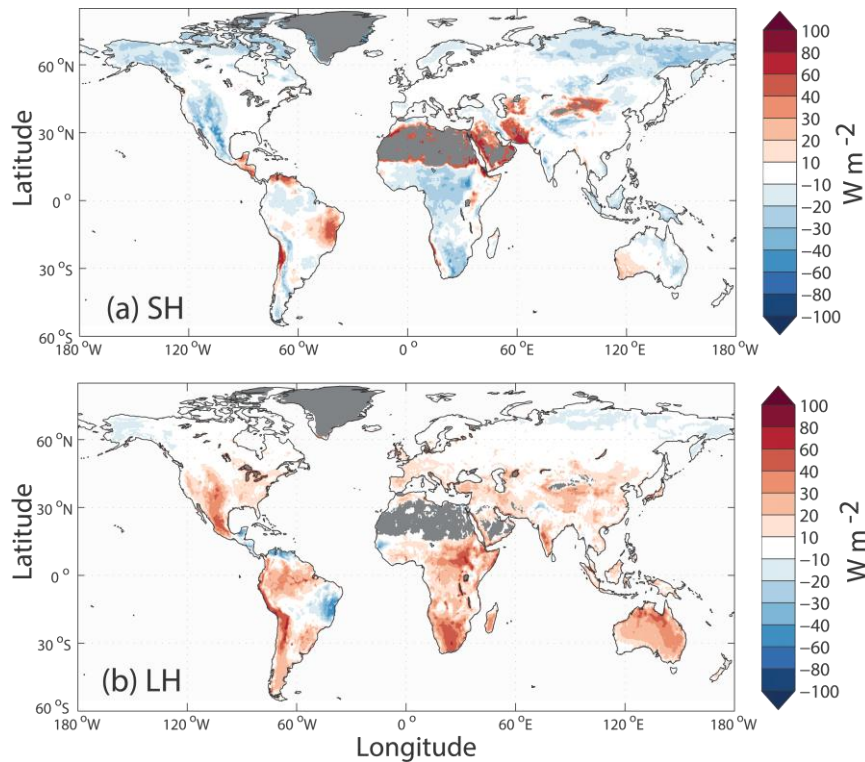


Figure S6. The difference in fluxes of sensible heat (SH; a) and latent heat (LH; b) between the period 1976–2005 from the Hist1 (1976–2005) experiment from NorESM1-Happi and the period 1982–2005 from the FLUXNET Model Tree Ensembles (FLUXNET-MTE; Jung et al., 2011). Areas with missing observations are shaded with dark grey colour. Units are W m^{-2} (a-b).

Comments: The FLUXNET-MTE estimates are restricted to vegetated land surfaces. The simulated sensible heat flux is generally too small, while the latent heat flux, and thus the evaporation, is considerably overestimated over low-latitude land. This is consistent with the model’s overly low cloud fractions, which allow more solar radiation to reach the ground and cause evaporation (Table S6). The overestimates in Africa, America and Australia are reduced relative to NorESM1-M (Bentsen et al., 2013; Figure 5). The differences for sensible heat flux are minor.

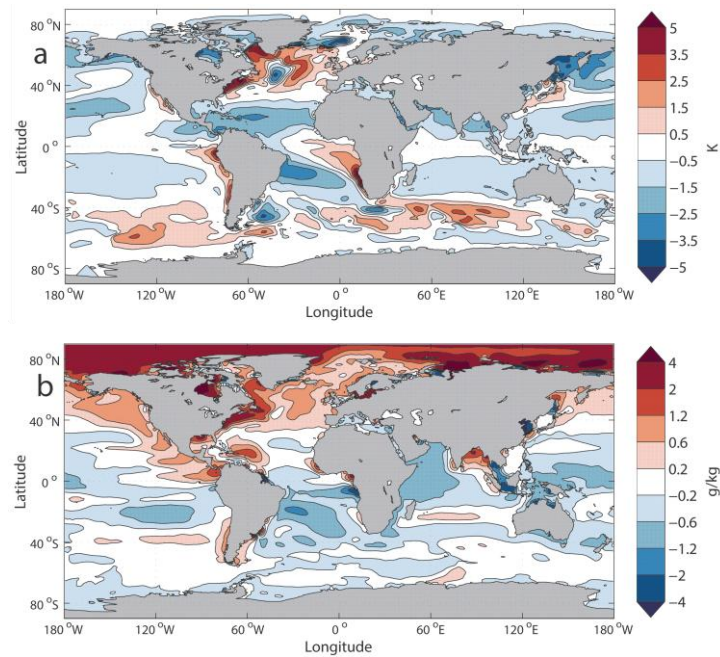


Figure S7. Differences in sea-surface temperature (SST; a) and sea-surface salinity (SSS; b) between the Hist1 experiment (1976–2005) from NorESM1-Happi and observation-based data obtained from WOA09 (Locarnini et al., 2010; Antonov et al., 2010). Units are K (a) and g kg^{-1} (b).

Comments: As for the continents (Fig. S5), the cold bias dominates the SST, except along the SH extratropical storm track, along the upwelling zones to the west of South America, and in the north-west and southeast Atlantic Ocean. The magnitude of the positive biases is reduced in NorESM1-Happi compared to NorESM1-M (Bentsen et al., 2013; Figure 12b), while the negative biases are comparable. The pattern of the SSS biases is almost the same as for NorESM1-M (Fig 12c in Bentsen et al, 2013). SSS is considerably overestimated at high latitudes in the NH, and underestimated in the tropics and sub-tropics. This pattern of SSS changes may contribute to a strengthened thermohaline forcing of AMOC.

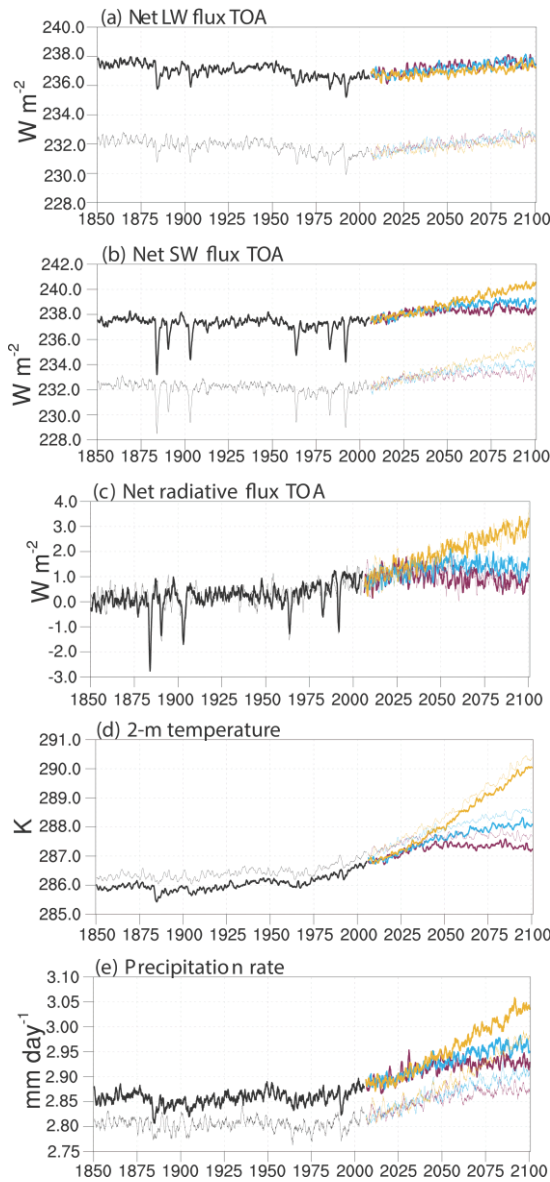


Figure S8. Time-evolution of global-mean monthly values of net longwave (positive upward; a), shortwave (positive downward, b), and total radiative flux (positive downward; c), all at the top of the atmosphere; and the near-surface temperature (d), and precipitation rate (e) for Hist1 (1850–2005; black), RCP2.6 (2006–2100; green), RCP4.5 (2006–2100; blue), and RCP8.6 (2006–2100; purple) from NorESM1-Happi (thick curves) and NorESM1-M (thin curves). Units are W m^{-2} (a–b), K (c) and mm day^{-1} (d).

Comments: The larger TOA influx of SW radiation in NorESM1-Happi than in NorESM1-M is almost entirely compensated by increased TOA outgoing LW radiation, and more than 20 % of this increase is from the clear sky (Table S2). The net radiative imbalance in the two models is almost identical from 1850 to 2100. Nevertheless, the global-mean near-surface temperature is lower by approximately 0.3 K in NorESM1-Happi. The global precipitation rate is about 0.06 mm d^{-1} higher (Table S4), consistent with the higher latent heat flux (Table S2).

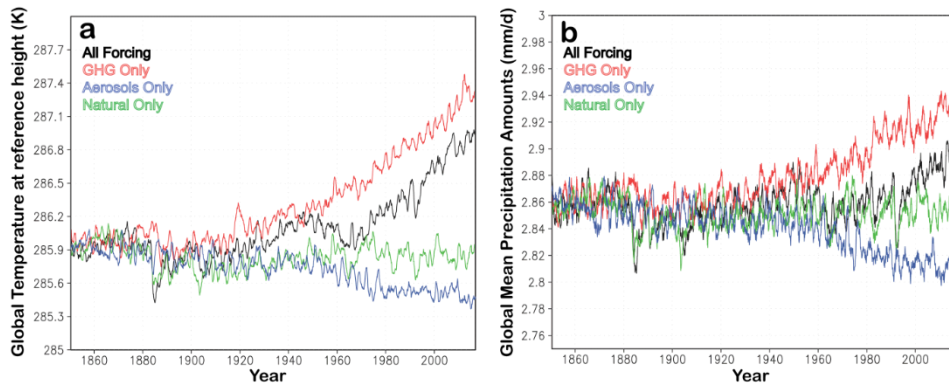


Figure S9. Time-evolution of global-mean near-surface temperature (a) and daily precipitation amounts (b) over the historical period (1850–2015) for the All forcing (black), greenhouse gas concentrations (GHG) only (red), Aerosol only (blue), and Natural forcing only (green) experiments with NorESM1-Happi. All Forcing is the regular Hist1 simulation; GHG only has varying greenhouse gas concentrations but all other forcings held constant at 1850 levels; Aerosol only has varying aerosol emissions but all other forcings held constant at 1850 levels in 1850; and Natural forcing only has varying natural contributions but all other forcings held constant at 1850 levels. Units are K (a) and mm day⁻¹ (b).

Comments: The simulated warming since the 1970s (black) cannot be reproduced with natural forcing only (green). The GHGs alone (red) lead to exaggerated warming. The aerosols (blue) significantly dampen the warming. The signals for global precipitation follow those for temperature, but are smaller. As discussed in Iversen et al. (2013), the regional variations in the simulated precipitation changes are crucial, since a more intense hydrological cycle in a warmer climate leads to reduced precipitation in some regions periods and more intense precipitation events in others (Giorgi et al., 2011).

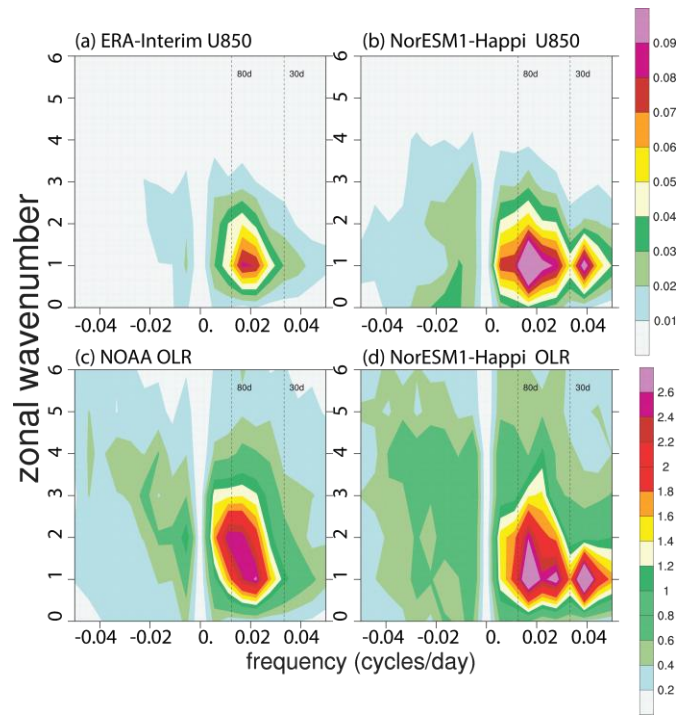


Figure S10. November–April wavenumber–frequency spectra for 10°S – 10°N computed from daily-mean zonal winds at 850 hPa from ERA-Interim (Dee et al., 2011; a) and the Hist1 experiment from NorESM1-Happi (b), and daily outgoing long-wave radiation (OLR) from NOAA satellite (c) and Hist1 with NorESM1-Happi (d). We use years 1979–2008 from ERA-Interim, 1979–2008 from the NOAA satellite, and 1976–2005 from NorESM1-Happi. Individual spectra were calculated for each year and then averaged over all years of data. The climatological seasonal cycle and time-mean for each November–April segment were removed before calculation of the spectra. The band-width is 180 day^{-1} . Units are m s^{-2} (a-b) and $\text{W m}^{-2} \text{ s}^{-1}$ (c-d) per frequency interval per wavenumber interval.

Comments: The Madden–Julian oscillation (MJO), an eastward propagation of planetary scale clusters of deep convection in the tropics, is the dominant mode of 30–90-day variability in the tropical atmosphere (Madden and Julian, 1971; Zhang, 2005). The CCSM4 was one of the first global climate models to have a fair representation of the MJO (Subramanian et al., 2011). The figure shows a diagnostic of the MJO as simulated by the model and from the ERA-Interim and NOAA data, taken as observations. The model has a clear signature of the MJO with a clear maximum between 40 and 60 days for wavenumber 1. The spectra are particularly improved compared to NorESM1-M for OLR (Bentsen et al., 2013; Figure 19), although there is still too much energy at periods shorter than a month.

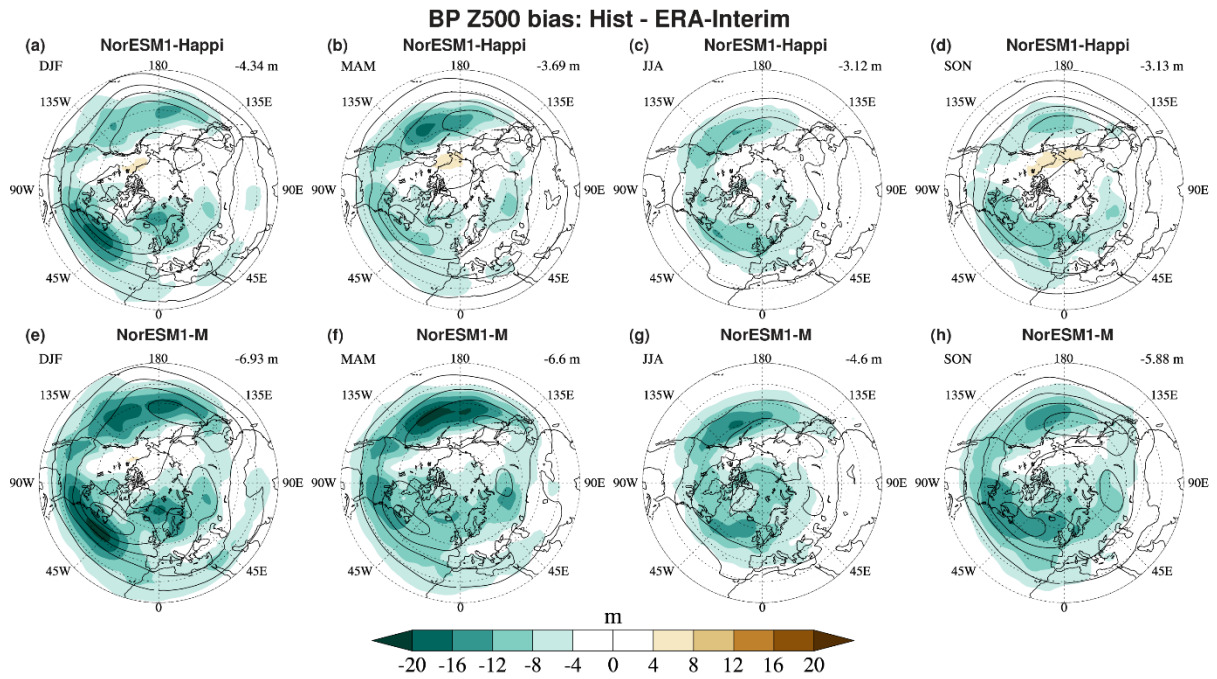


Figure S11. NH extratropical baroclinic wave activity (storm track) biases relative to ERA-Interim (colors) and mean climatology (solid black; 8 to 72 m in increments of 8 m) from the three historical simulations (Hist1, Hist2, and Hist2) from NorESM1-Happi (top; a-d) and NorESM1-M (bottom; e-h). Fields are shown for December-February (DJF; a, e), March-May (MAM; b, f), June-August (JJA; c, g), and September-November (SON; d, h). The baroclinic wave activity is estimated as the standard deviation of the bandpass time-filtered geopotential height at 500 hPa, retaining periods of 2.5–6 days (Blackmon, 1976). We use years 1976–2005 from NorESM1-M and NorESM1-Happi and 1979–2008 from ERA-Interim. Units are m (a-h).

Comments: Extratropical cyclones are important vehicles for the atmospheric meridional transport of heat, humidity and momentum in the mid-latitudes, and for the maintenance of the eddy-driven polar jet (e.g. Bratseth, 2001; 2003). Eddy activity is underestimated in all seasons in both model versions. The magnitude of the bias is considerably reduced in NorESM1-Happi in all seasons, and in particular over the Pacific Ocean. It is also reduced in the region where the North-Atlantic cyclones travel into the Nordic Seas towards the Arctic, which is important for the geographical distribution of the wind- and precipitation-climate in the European-Atlantic sector. The underestimation during the North Atlantic winter is, however, considerable in NorESM1-Happi. The improvements in NorESM1-Happi are probably due to the higher spatial resolution (e.g. Jung et al., 2012).

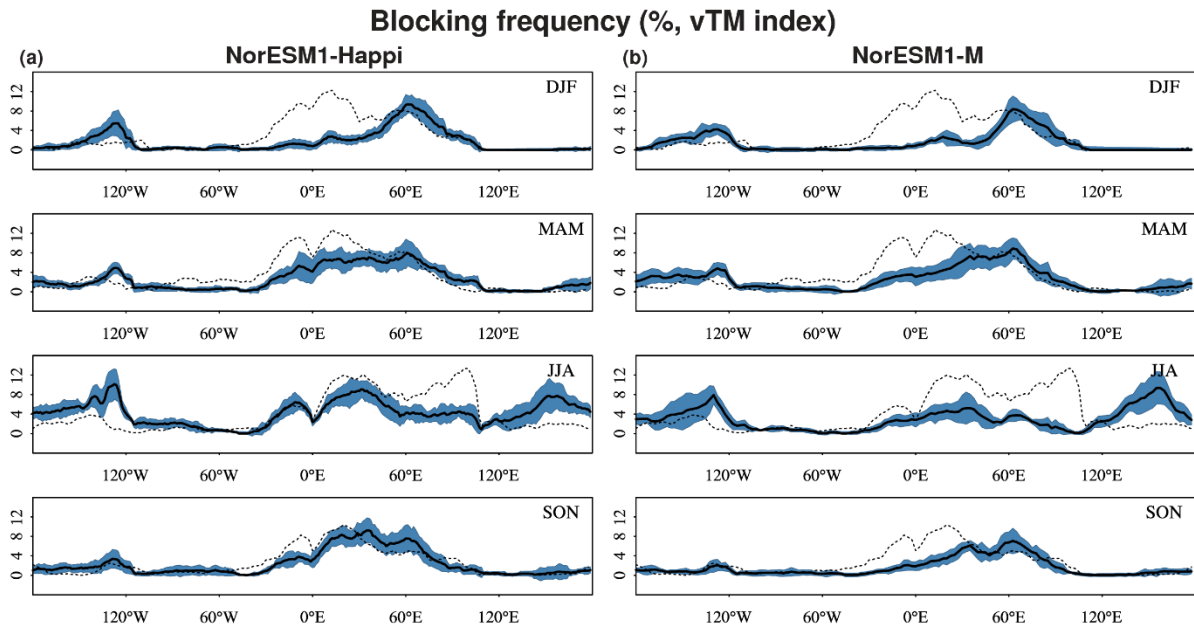


Figure S12. NH blocking frequency for the three historical simulations (Hist1, Hist2, and Hist3) from NorESM1-Happi (a) and NorESM1-M (b) for years 1976–2005. The solid black curves represent the ensemble mean and the blue shading is the ensemble spread (\pm one standard deviation) from the model. The dotted black curves are for the ERA-Interim data for the period 1979–2008 (Dee et al., 2011). The seasonal occurrence of blocking is based on the 500 hPa vTM-index (Tibaldi and Molteni, 1990) relative to the latitudes of the average position of the baroclinic wave activity by season (Fig. S11; Pelly and Hoskins, 2002; see also Iversen et al., 2013). Units are % (a–b).

Comments: For blocking, NorESM1-Happi also shows better results than NorESM1-M. Still, important systematic errors persist in several sectors and seasons. The best results are seen in the autumn (September–November; SON), when the blocking occurrence is close to perfect at all longitudes except for an underestimate over the North Atlantic Ocean. The errors are also moderate during spring (March–May; MAM), while in winter, both model versions severely underestimate blocking in the Atlantic-European sector. In summer (July–August; JJA), blocking over Europe is well represented, but it is underestimated over central Eurasia and overestimated in the Pacific sector. As discussed in Iversen et al. (2013), several studies point to poor model resolution as an explanation for systematic errors in blocking occurrence (see also Dawson et al., 2012; Davini and D’Andrea, 2016; and Woolings et al., 2018). Since extratropical blocking is connected with persistent anomalous patterns of precipitation at mid-latitudes, this causes systematic errors in the simulated climate.

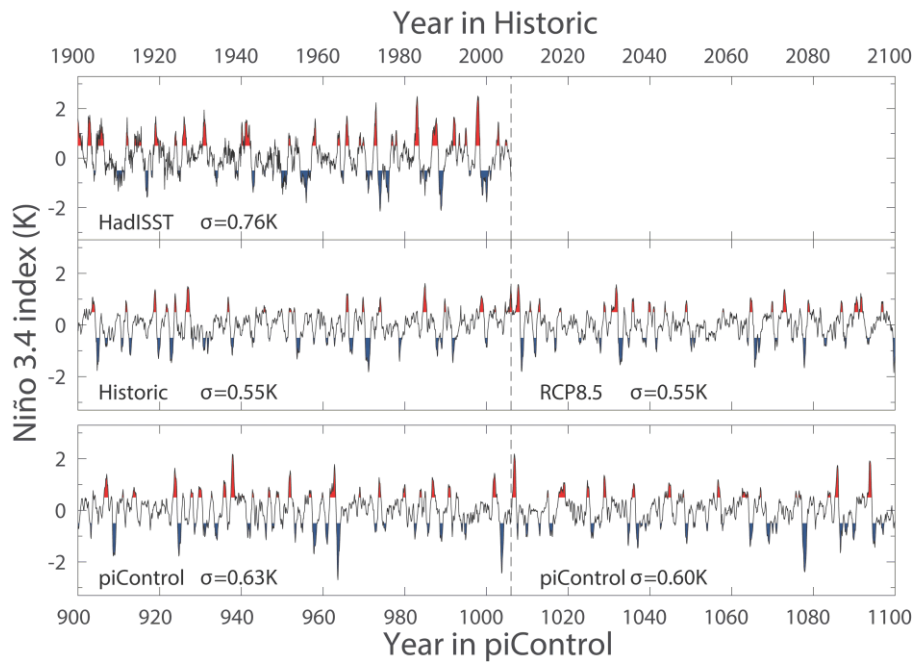


Figure S13. Time-evolution of detrended monthly anomalies in sea-surface temperature (SST) of the Niño3.4 region (5°S – 5°N ; 170°W – 120°W) for the Hadley Centre Sea Ice and SST data set (HadISST; Rayner et al., 2003) for the period 1900–2005 (top), the Hist1 experiment (1900–2005) and RCP8.5 (2006–2100) from NorESM1-Happi (middle), and the piControl experiment (900–1100) from NorESM1-Happi (bottom). The anomalies are calculated relative to the mean over the entire time series for each month. Red (blue) colours indicate that anomalies are larger (smaller) than $+0.4\text{ K}$ (-0.4 K), see Trenberth (1997) for recommendations. Units are K.

Comments: The El Niño–Southern Oscillation (ENSO) involves ocean–atmosphere interactions in the tropical Pacific on seasonal to inter-annual timescales (Wallace et al., 1998), with a strong association to global scale patterns (Trenberth et al., 1998; Straus and Shukla, 2002). NorESM1-M was amongst 9 out of 20 CMIP5 models that reproduced both the two flavours of ENSO variability, over the central and eastern tropical Pacific Ocean (Kim and Yu, 2012). The temporal standard deviation of the time series from NorESM1-Happi (NorESM1-M in brackets) is 0.55 K (0.92 K) for Hist1 and 0.63 (0.86 K) for piControl. The value from HadISST is 0.75 K, which is larger than that from NorESM1-Happi but smaller than from NorESM1-M. The frequency of ENSO variability is reduced in NorESM1-Happi and closer to the HadISST.

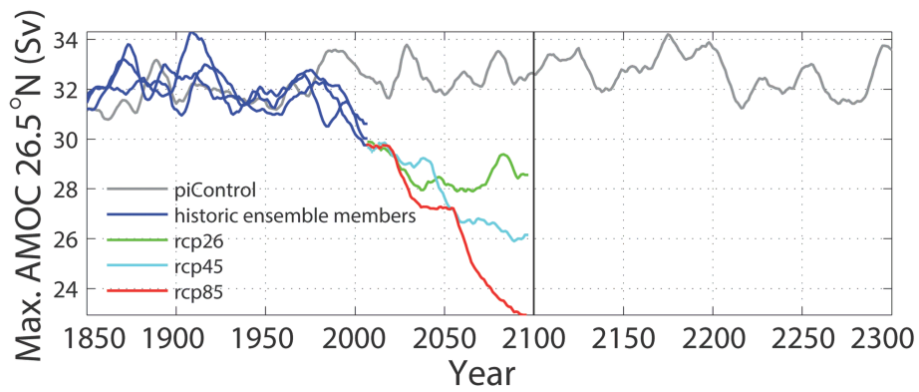


Figure S14. Decadal moving averages of the annual maximum Atlantic Meridional Overturning Circulation (AMOC) at 26.5°N from the piControl (1850–2005; grey), Hist1, Hist2, and Hist3 (1850–2005; blue), RCP2.6 (2006–2100; green), RCP4.5 (2006–2100; blue), and RCP8.5 (2006–2100; red) experiments with NorESM1-Happi. Units are Sv.

Comments: The very strong AMOC in NorESM1-Happi may be due to a strong thermohaline forcing associated with the fast cycling of fresh water and overestimated sea-surface salinity in the Arctic (Fig. S7). As for the near-surface air temperature (Fig. S8), it takes some decades before one notices considerable differences between the AMIP in the different RCPs. The AMOC in NorESM1-Happi is still stronger when approaching year 2100 in RCP8.5 than in the present climate in many other models.

Table S7. Three estimates of equilibrium climate sensitivity (ECS), two estimates of the overall feedback parameter, and two estimates of the transient climate response (TCR) from NorESM1-Happi, NorESM1-M (Iversen et al, 2013), and CCSM4 (Bitz et al., 2012). The estimates of ΔT_{eq} are calculated with the slab-ocean model NorESM1-HappiSO (experiments SO-2 \times CO₂ and SO-4 \times CO₂; see Table 2 and Sect. 2.1). ΔT_{reg} , the TOA radiative forcing $R_{f,reg}$, and the feedback parameter λ_{reg} are based on fully coupled model simulations with abrupt quadrupling of CO₂ (abrupt 4 \times CO₂; Table S1) following the method of Gregory et al. (2004). In accordance with Murphy (1995) ΔT_{eff} and $\lambda_{eff} = -R_{f0}/\Delta T_{eff}$ (Gettelman, 2012) are calculated assuming negligible slow feedback contributions, and $R_{f0} = 3.5 \text{ W m}^{-2}$ (Kay et al., 2012). The transient values, ΔT_{TCR} and $\Delta T_{TCR,eff}$, are calculated from experiments where CO₂ concentrations are increased 1 % per year until quadrupling (gradual 4 \times CO₂; Table S1).

Model	ΔT_{eq} K	ΔT_{eff} K	ΔT_{reg} K	$R_{f,reg}$ W m ⁻²	λ_{reg} W m ⁻² K ⁻¹	λ_{eff} W m ⁻² K ⁻¹	ΔT_{TCR} K	$\Delta T_{TCR,eff}$ K
CCSM4 1 deg.	3.20	2.78	2.80	2.95	-1.053	-1.260	1.72	2.64
NorESM1-M 2 deg.	3.50	2.86	2.86	3.17	-1.108	-1.224	1.37	2.29
NorESM1-Happi 1 deg.	3.34	2.87	2.82	3.43	-1.214	-1.220	1.52	2.47

Comments: NorESM1-Happi is less sensitive than NorESM1-M and slightly more sensitive than CCSM4. The independent estimate of the TOA radiative forcing ($R_{f0} = 3.5 \text{ W m}^{-2}$; Kay et al., 2012) is larger than regression estimates for all three models, although the difference for NorESM1-Happi is much smaller. This difference is normally ascribed to fast feedbacks during the first year while the difference between ΔT_{reg} and ΔT_{eq} reflects the error of using linear regression due to slow feedbacks e.g. in the oceans (Senior and Mitchell, 2000). Different estimates of the effective feedback parameter λ_{eff} are more internally consistent than those of λ_{reg} , and we consider $-1.22 \text{ W m}^{-2} \text{ K}^{-1}$ to be the more reliable estimate. For the three models, ΔT_{reg} and ΔT_{eff} are almost equal and the models are less sensitive than most of the CMIP5 models (e.g. Andrews et al., 2012). While the approximate values for ECS are close, the values for TCR differ, and NorESM1-M has the smallest values.

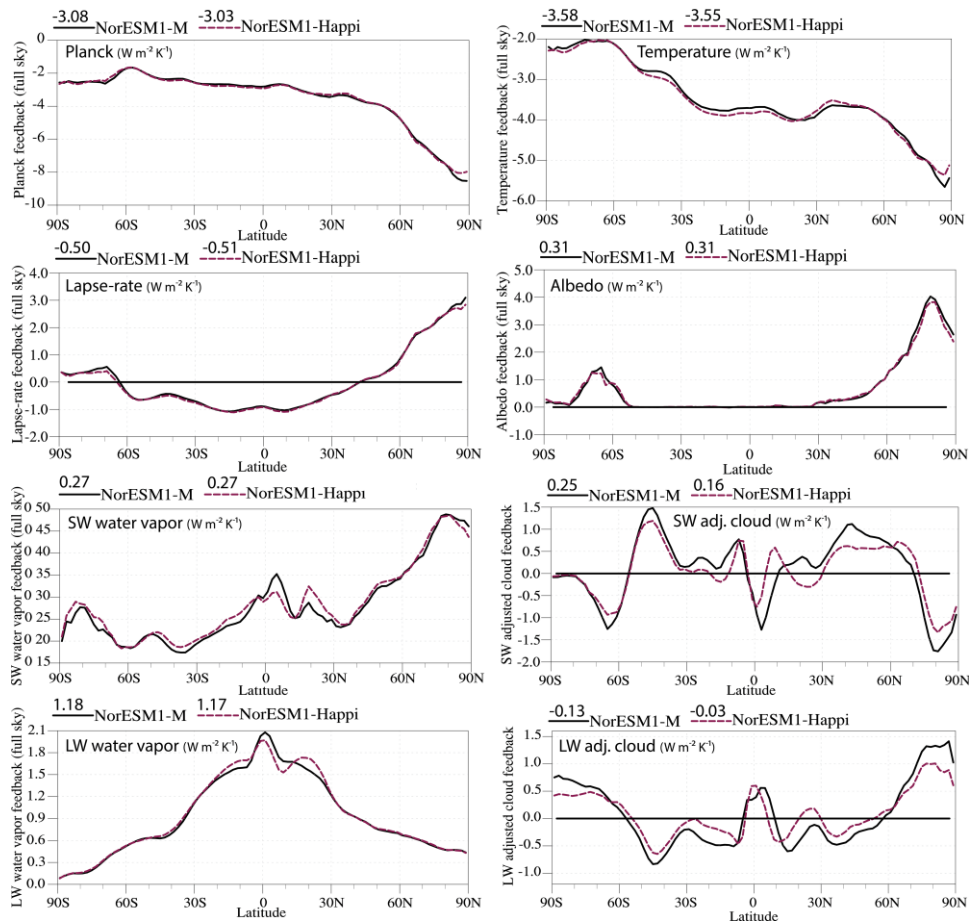


Figure S15. Zonal-mean physical contributions to the feedback parameter from the Planck feedback (top row, left), temperature feedback (top row, right), lapse-rate feedback (second row, left), albedo feedback (second row, right), short-wave (SW) and long-wave (LW) water vapour feedbacks (third and fourth row, left), and the SW and LW adjusted water vapour feedbacks (third and fourth row, right). The feedbacks are defined as in Soden et al. (2008) and calculated from the abrupt $4\times\text{CO}_2$ experiments with NorESM1-Happi (solid black curve) and NorESM1-M (dashed purple curve), applying the radiative kernel method (Soden and Held, 2006; Soden et al., 2008; Gettelman et al., 2012). The kernels are from the GFDL atmospheric model (AM2p12b) using climatological and seasonally varying sea surface temperatures and sea ice, and the adjusted values for clouds account for changes in the cloud radiative forcing due to changes in the other feedback variables (Soden et al. 2008). Global averages are given above each panel. The temperature feedback is the sum of the Planck and Lapse Rate feedbacks. Units are $\text{W m}^{-2} \text{K}^{-1}$.

Comments: Neglecting nonlinear contributions, the total feedback parameter is estimated as the sum of the physical contributions, which gives a value of $-1.67 \text{ W m}^{-2} \text{K}^{-1}$ for NorESM1-Happi ($-1.71 \text{ W m}^{-2} \text{K}^{-1}$ for NorESM1-M). This differs considerably from the effective values in Table S7. A radiative kernel calculation with the slab-ocean model (NorESM1-HappiSO) between equilibrated climate states, gives $-1.40 \text{ W m}^{-2} \text{K}^{-1}$. Assuming that the regression method (Gregory et al., 2004) is approximately consistent with the radiative kernel method, this indicates that the difference $0.27 \text{ W m}^{-2} \text{K}^{-1}$ can be ascribed to slow deep ocean feedbacks (Proistosescu and Huybers, 2017), and a residue of $0.17 \text{ W m}^{-2} \text{K}^{-1}$ is due to nonlinearity. The curves show that the albedo, lapse-rate feedbacks, and to some extent the short-wave water-vapour feedbacks, contribute to the Arctic amplification of the temperature response to increased CO_2 concentrations.

References

- Adler, R. F., Huffman, G. J., Chang, A., Ferraro, R., Xie, P., Janowiak, J., Rudolf, B., Schneider, U., Curtis, S., Bolvin, D., Gruber A., Susskind, J., and Arkin, P.: The Version 2 Global Precipitation Climatology Project (GPCP) Monthly Precipitation Analysis (1979–Present), *J. Hydrometeor.*, 4, 1147–1167, [https://doi.org/10.1175/1525-7541\(2003\)004%3C1147:TVGPCP%3E2.0.CO;2](https://doi.org/10.1175/1525-7541(2003)004%3C1147:TVGPCP%3E2.0.CO;2), 2003.
- Ammann, C. M., Meehl, G. A., Washington, W. M., and Zender, C.: A monthly and latitudinally varying volcanic forcing dataset in simulations of 20th century climate. *Geophys. Res. Lett.*, 30, 1657, <https://doi.org/10.1029/2003GL016875>, 2003
- Andrews, T., Gregory, J. M., Webb, M. J., and Taylor, K. E.: Forcing, feedbacks and climate sensitivity in CMIP5 coupled atmosphere-ocean climate models. *Geophys. Res. Lett.*, 39, L09712, <https://doi.org/10.1029/2012gl051607>, 2012.
- Antonov, J. I., Seidov, D., Boyer, T. P., Locarnini, R. A., Mishonov, A. V., Garcia, H. E., Baranova, O. K., Zweng, M. M., and Johnson, D. R.: World Ocean Atlas 2009, Volume 2: Salinity, in: NOAA Atlas NESDIS 69, edited by: Levitus, S., U.S. Government Printing Office, Washington, DC, 184 pp., 2010.
- Bentsen, M., Bethke, I., Debernard, J. B., Iversen, T., Kirkevåg, A., Seland, Ø., Drange, H., Roelandt, C., Seierstad, I. A., Hoose, C., Kristjánsson, J. E.: The Norwegian Earth System Model, NorESM1-M—Part 1: Description and basic evaluation of the physical climate. *Geosci. Model Dev.*, 6, 687–720, <https://doi.org/10.5194/gmd-6-687-2013>, 2013.
- Bitz, C. M., Shell, K. M., Gent, P. R., Bailey, D. A., Danabasoglu, G., Armour, K. C., Holland, M. M., Kiehl, J. T.: Climate Sensitivity of the Community Climate System Model, Version 4. *J. Climate*, 25, 3053–3070, <http://dx.doi.org/10.1175/JCLI-D-11-00290.1>, 2012.
- Blackmon, M. L.: A climatological spectral study of the 500 mb geopotential height of the Northern Hemisphere. *J. Atmos. Sci.*, 33, 1607–1623, [https://doi.org/10.1175/1520-0469\(1976\)033%3C1607:ACSSOT%3E2.0.CO;2](https://doi.org/10.1175/1520-0469(1976)033%3C1607:ACSSOT%3E2.0.CO;2), 1976.
- Bretherton, C. S., Widmann, M., Dymnikov, V. P., Wallace, J. M., and Bladé, I.: The effective number of spatial degrees of freedom of a time-varying field, *J. Climate*, 12, 1990–2009, [https://doi.org/10.1175/1520-0442\(1999\)012%3C1990:TENOSD%3E2.0.CO;2](https://doi.org/10.1175/1520-0442(1999)012%3C1990:TENOSD%3E2.0.CO;2), 1999.
- Bratseth, A. M.: Eddy Acceleration of the Mean Flow in the Atmosphere. *J. Atmos. Sci.*, 58, 3328–3339, [https://doi.org/10.1175/1520-0469\(2001\)058%3C3328:EAOTMF%3E2.0.CO;2](https://doi.org/10.1175/1520-0469(2001)058%3C3328:EAOTMF%3E2.0.CO;2), 2001.
- Bratseth, A. M.: Zonal-mean transport characteristics of ECMWF re-analysis data. *Q. J. R. Meteorol. Soc.*, 129, 2331–2346. <https://doi.org/10.1256/qj.02.90>, 2003.
- Collins, W. D., Rasch, P. J., Boville, B. A., Hack, J. J., McCaa, J. R., Williamson, D. L., and Briegleb, B. P.: The formulation and atmospheric simulation of the community atmosphere model version, *J. Climate*, 19, 2144–2161, 2006.
- Dawson, A., Palmer, T. N., and Corti, S.: Simulating regime structures in weather and climate prediction models. *Geophys. Res. Lett.*, 39, L21805, <https://doi.org/10.1029/2012GL053284>, 2012.
- Davini P. and D’Andrea F. Northern Hemisphere atmospheric blocking representation in global climate models: twenty years of improvements? *J. Climate*, 29, 8823–8840, <https://doi.org/10.1175/JCLI-D-16-0242.1>, 2016.
- Dee, D. P., Uppala, S. M., Simmons, A. J., Berrisford, P., Poli, P., Kobayashi, S., Andrae, U., Balmaseda, M. A., Balsamo, G., Bauer, P., Bechtold, P., Beljaars, A. C. M., van de Berg, L., Bidlot, J., Bormann, N., Delsol,

- C., Dragani, R., Fuentes, M., Geer, A. J., Haimberger, L., Healy, S. B., Hersbach, H., Hólm, E. V., Isaksen, L., Kållberg, P., Köhler, M., Matricardi, M., McNally, A. P., Monge-Sanz, B. M., Morcrette, J.-J., Park, B.-K., Peubey, C., de Rosnay, P., Tavolato, C., Thépaut, J.-N. and Vitart, F., The ERA-Interim reanalysis: configuration and performance of the data assimilation system. *Q. J. R. Meteorol. Soc.*, 137, 553–597. <https://doi.org/10.1002/qj.828>, 2011.
- Gent, P.R., Danabasoglu, G., Donner, L. J., Holland, M. M., Hunke, E. C., Jayne, S. R., Lawrence, D. M., Neale, R. B., Rasch, P. J., Vertenstein, M., Worley, P. H., Yang, Z.-L., and Zhang, M.: The Community Climate System Model Version 4, *J. Climate*, 24, 4973–4991, <https://doi.org/10.1175/2011JCLI4083.1>, 2011.
- Gettelman, A., Kay, J. E., Shell, K. M.: The Evolution of Climate Sensitivity and Climate Feedbacks in the Community Atmosphere Model. *J. Climate*, 25, 1453–1469, <http://dx.doi.org/10.1175/JCLI-D-11-00197.1>, 2012.
- Giorgi, F., Im, E.-S., Coppola, E., Diffenbaugh, N. S., Gao, X. J., Mariotti, L., and Shi, Y.: Higher Hydroclimatic Intensity with Global Warming. *J. Climate*, 24, 5309–5324, <https://doi.org/10.1175/2011JCLI3979.1>, 2011.
- Gregory, J. M., Ingram, W. J., Palmer, M. A., Jones, G. S., Stott, P. A., Thorpe, R. B., Lowe, J. A., Johns, T. C., and Williams, K. D.: A new method for diagnosing radiative forcing and climate sensitivity, *Geophys. Res. Lett.*, 31, L03205, <https://doi.org/10.1029/2003GL018747>, 2004.
- Hansen, J., Ruedy, R., Sato, M., and Lo, K.: Global surface temperature change. *Rev. Geophys.*, 48, RG4004, <https://doi.org/10.1029/2010RG000345>, 2010.
- Harrison, E. F., Minnis, P., Barkstrom, B. R., Ramanathan, V., Cess, R. D., and Gibson, G. G.: Seasonal variation of cloud radiative forcing derived from the earth radiation budget experiment, *J. Geophys. Res.*, 95, 18687–18703, 1990.
- Huffman, G. J., Adler, R. F., Bolvin, D. T., and Gu, G.: Improving the global precipitation record: GPCP Version 2.1, *Geophys. Res. Lett.*, 36, L17808, <https://doi.org/10.1029/2009GL040000>, 2009.
- Hurrell, J. W., Hack, J. J., Shea, D., Caron, J. M., and Rosinski, J.: A New Sea Surface Temperature and Sea Ice Boundary Dataset for the Community Atmosphere Model. *J. Climate*, 21, 5145–5153, <doi.org/10.1175/2008JCLI2292.1>, 2008.
- Iversen, T., Bentsen, M., Bethke, I., Debernard, J. B., Kirkevåg, A., Seland, Ø., Drange, H., Kristjansson, J. E., Medhaug, I., Sand, M., and Seierstad, I. A.: The Norwegian Earth System Model, NorESM1-M – Part 2: Climate response and scenario projections, *Geosci. Model Dev.*, 6, 389–415, <https://doi.org/10.5194/gmd-6-389-2013>, 2013.
- Jiang, J.H., Su, H, Zhai, C., Perun, V.S and co-authors: Evaluation of Cloud and Water Vapor Simulations in CMIP5 Climate Models Using NASA "A-Train" Satellite Observations, *J. Geophys. Res.*, 117, D14105, 24 pp., <https://doi.org/10.1029/2011JD017237>, 2012.
- Jung, T., Miller, M. J., Palmer, T. N., Towers, P., Wedi, N., Achuthavarier, D., Adams, J. M., Alshuler, E. L., Cash, B. A., Kinter III, J. L., Marx, L., Stan, C., and Hodges, K. I.: High-Resolution Global Climate Simulations with the ECMWF Model in Project Athena: Experimental Design, Model Climate, and Seasonal Forecast Skill, *J. Climate*, 25, 3155–3172, <http://dx.doi.org/10.1175/JCLI-D-11-00265.1>, 2012.
- Jung, M., Reichstein, M., Margolis, H. A., Cescatti, A., Richardson, A. D., Arain, M. A., Arneth, A., Bernhofer, C., Bonal, D., Chen, J., Gianelle, D., Gobron, N., Kiely, G., Kutsch, W., Lasslop, G., Law, B. E., Lindroth, A., Merbold, L., Montagnani, L., Moors, E. J., Papale, D., Sottocornola, M., Vaccari, F., and

- Williams, C.: Global patterns of land-atmosphere fluxes of carbon dioxide, latent heat, and sensible heat derived from eddy covariance, satellite, and meteorological observations, *J. Geophys. Res.*, 116, G00J07, <https://doi.org/10.1029/2010JG001566>, 2011.
- Kanamitsu, M., Ebisuzaki, W., Woollen, J., Yang, S. K., Hnilo, J. J., Fiorino, M., and Potter, G. L.: NCEP-DOE AMIP-II reanalysis (R-2), *Bull. Amer. Meteor. Soc.*, 83, 1631–1643, <https://doi.org/10.1175/BAMS-83-11-1631>, 2002.
- Kay, J. E., Holland, M. M., Bitz, C.M., Blanchard-Wrigglesworth, E., Gettelman, A., Conley, A., and Bailey, D.: The influence of local feedbacks and northward heat transport on the equilibrium Arctic climate response to increased greenhouse gas forcing. *J. Climate*, early online release, <http://dx.doi.org/10.1175/JCLI-D-11-00622.1>, 2012.
- Kiehl, J. T. and Trenberth, K. E.: Earth's annual global mean energy budget, *Bull. Amer. Meteor. Soc.*, 78, 197–208, [https://doi.org/10.1175/1520-0477\(1997\)078%3C0197:EAGMEB%3E2.0.CO;2](https://doi.org/10.1175/1520-0477(1997)078%3C0197:EAGMEB%3E2.0.CO;2), 1997.
- Kim, S. T. and Yu, J-Y.: The Two Types of ENSO in CMIP5 Models, *Geophys. Res. Lett.*, 39, L11704, <https://doi.org/10.1029/2012GL052006>, 2012.
- Kirkevåg, A., Iversen, T., Seland, Ø., Hoose, C., Kristjánsson, J. E., Struthers, H., Ekman, A. M. L., Ghan, S., Griesfeller, J., Nilsson, E. D., and Schulz, M.: Aerosol–climate interactions in the Norwegian Earth System Model – NorESM1-M, *Geosci. Model Dev.*, 6, 207–244, <https://doi.org/10.5194/gmd-6-207-2013>, 2013.
- Large, W. G. and Yeager, S.: Diurnal to decadal global forcing for ocean and sea ice models: the data sets and flux climatologies, Tech. Rep. NCAR/TN-460+STR, National Center for Atmospheric Research, Boulder, Colorado, USA, 2004.
- Lean, J., Rottman, G., Harder, J., and Kopp, G.: *SORCE contributions to new understanding of global change and solar variability*, *Sol. Phys.*, 230, 27–53, https://doi.org/10.1007/0-387-37625-9_3, 2005.
- L'Ecuyer, T. S., Wood, N. B., Haladay, T., Stephens, G. L., and Stackhouse Jr., P. W.: Impact of clouds on atmospheric heating based on the R04 CloudSat fluxes and heating rates data set, *J. Geophys. Res.*, 113, D00A15, <https://doi.org/10.1029/2008JD009951>, 2008.
- Legates, D. R. and Willmott, C. J.: Mean seasonal and spatial variability in gauge-corrected, global precipitation, *Int. J. Climatol.*, 10, 111–127, <https://doi.org/10.1002/joc.3370100202>, 1990.
- Locarnini, R. A., Mishonov, A. V., Antonov, J. I., Boyer, T. P., Garcia, H. E., Baranova, O. K., Zweng, M. M., and Johnson, D. R.: *World Ocean Atlas 2009, Volume 1: Temperature*, in: NOAA Atlas NESDIS 68, edited by: Levitus, S., US Government Printing Office, Washington, D.C., 184 pp., 2010.
- Loeb, N. G., Kato, S., Loukachine, K., and Manalo-Smith, N.: Angular distribution models for top-of-atmosphere radiative flux estimation from the clouds and the earths radiant energy system instrument on the Terra satellite, Part I: Methodology, *J. Atmos. Ocean. Tech.*, 22, 338–351, <https://doi.org/10.1175/JTECH1712.1>, 2005.
- Loeb, N. G., Wielicki, B. A., Doelling, D. R., Smith, G. L., Keyes, D. F., Kato, S., Manalo-Smith, N., and Wong, T.: Toward optimal closure of the earth's top-of-atmosphere radiation budget, *J. Climate*, 22, 748–766, <https://doi.org/10.1175/2008JCLI2637.1>, 2009.
- Loeb, N. G., Lyman, J. M., Johnson, G. C., Allan, R. P., Doelling, D. R., Wong, T., Soden, B. J., and Stephens, G. L.: Observed changes in top-of-the-atmosphere radiation and upper-ocean heating consistent within uncertainty, *Nat. Geosci.*, 5, 110–113, <https://doi.org/10.1038/ngeo1375>, 2012.

- Madden, R. A. and Julian, P. R.: Detection of a 40–50 day oscillation in the zonal wind in the Tropical Pacific, *J. Atmos. Sci.*, 28, 702–708, [https://doi.org/10.1175/1520-0469\(1971\)028%3C0702:DOADOI%3E2.0.CO;2](https://doi.org/10.1175/1520-0469(1971)028%3C0702:DOADOI%3E2.0.CO;2), 1971.
- Mitchell, T. D. and Jones, P. D.: An improved method of constructing a database of monthly climate observations and associated high-resolution grids, *Int. J. Climatol.*, 25, 693–712, <https://doi.org/10.1002/joc.1181>, 2005.
- Morice, C. P., Kennedy, J. J., Rayner, N. A., and Jones, P. D.: Quantifying uncertainties in global and regional temperature change using an ensemble of observational estimates: the HadCRUT4 data set, *J. Geophys. Res.*, 117, D08101, <https://doi.org/10.1029/2011JD017187>, 2012.
- Murphy, D. M.: Transient response of the Hadley Centre coupled ocean-atmosphere model to increasing carbon dioxide: Part III. Analysis of global-mean response using simple models, *J. Climate*, 8, 495–514. [http://dx.doi.org/10.1175/1520-0442\(1995\)008<0496:TROTHC>2.0.CO;2](http://dx.doi.org/10.1175/1520-0442(1995)008<0496:TROTHC>2.0.CO;2), 1995.
- O’Dell, C. W., Wentz, F. J., and Bennartz, R.: Cloud liquid water path from satellite-based passive microwave observations: a new climatology over the global oceans, *J. Climate*, 21, 1721–1739, <https://doi.org/10.1175/2007JCLI1958.1>, 2008.
- Onogi, K., Tsutsui, J., Koide, H., Sakamoto, M., Kobayashi, S., Hatsushika, H., Matsumoto, T., Yamazaki, N., Kamahori, H., Takahashi, K., Kadokura, S., Wada, K., Kato, K., Oyama, R., Ose, T., Mannoji, N., and Taira, R.: The JRA-25 reanalysis, *J. Meteor. Soc. Jpn.*, 85, 369–432, <https://doi.org/10.2151/jmsj.85.369>, 2007.
- OSI-SAF, 2017: EUMETSAT Ocean and Sea Ice Satellite Application Facility. Global sea ice concentration climate data record 1979-2015 (v2.0, 2017), [Online]. Norwegian and Danish Meteorological Institutes. https://doi.org/10.15770/EUM_SAF_OSI_0008.
- Pelly, J. L. and Hoskins, B. J.: A new perspective on blocking, *J. Atmos. Sci.*, 60,743–755, [https://doi.org/10.1175/1520-0469\(2003\)060%3C0743:ANPOB%3E2.0.CO;2](https://doi.org/10.1175/1520-0469(2003)060%3C0743:ANPOB%3E2.0.CO;2), 2003.
- Proistosescu, C. and Huybers, P. J.: Slow climate mode reconciles historical and model-based estimates of climate sensitivity, *Sci. Adv.* 3, e1602821, <https://doi.org/10.1126/sciadv.1602821>, 2017.
- Rayner, N. A., Parker, D. E., Horton, E. B., Folland, C. K., Alexander, L. V., Rowell, D. P., Kent, E. C., and Kaplan, A.: Global analyses of sea surface temperature, sea ice, and night marine air temperature since the late nineteenth century, *J. Geophys. Res.*, 108 (D14), <https://doi.org/10.1029/2002JD002670>, 2003.
- Rossow, W. B. and Dueñas, E. N.: The International Satellite Cloud Climatology Project (ISCCP) web site: an online resource for research, *Bull. Amer. Meteor. Soc.*, 85, 167–172, <https://doi.org/10.1175/BAMS-85-2-167>, 2004.
- Rossow, W. B. and Schiffer, R. A.: Advances in understanding clouds from ISCCP, *Bull. Amer. Meteor. Soc.*, 80, 2261–2287, [https://doi.org/10.1175/1520-0477\(1999\)080%3C2261:AIUCFI%3E2.0.CO;2](https://doi.org/10.1175/1520-0477(1999)080%3C2261:AIUCFI%3E2.0.CO;2), 1999.
- Schwarz, J. P., Spackman, J. R., Gao, R. S., Watts, L. A., Stier, P., Schulz, M., Davis, S. M., Wofsy, S. C., and Fahey, D. W.: Global-scale black carbon profiles observed in the remote atmosphere and compared to models, *Geophys. Res. Lett.*, 37, L18812, <https://doi.org/10.1029/2010GL044372>, 2010
- Schwarz, J. P., Samset, B. H., Perring, A. E., Spackman, J. R., Gao, R. S., Stier, P., Schulz, M., Moore, F. L., Ray, E. A., and Fahey, D. W.: Global-scale seasonally resolved black carbon vertical profiles over the Pacific, *Geophys. Res. Lett.*, 40, 5542–5547, <https://doi.org/10.1002/2013gl057775>, 2013.

- Seland, Ø. and Debernard, J. B., Sensitivities of Arctic Sea ice in Climate Modelling, in: ACCESS Newsletter. No. 9, 10–13, http://www.access-eu.org/en/publications/access_newsletter.html, 2014.
- Senior, C. A. and Mitchell, J. F. B.: The time-dependence of climate sensitivity, *Geophys. Res. Lett.*, 27, 2685–2688. <https://doi.org/10.1029/2000GL011373>, 2000.
- Seethala, C. and Horvath, A.: Global assessment of AMSRE and MODIS cloud liquid water path retrievals in warm oceanic clouds, *J. Geophys. Res.*, 115, D13202, <https://doi.org/10.1029/2009JD012662>, 2010.
- Soden, B. J., and Held, I. M.: An assessment of climate feedbacks in coupled ocean–atmosphere models. *J. Climate*, 19, 3354–3360, <https://doi.org/10.1175/JCLI3799.1>, 2006.
- Soden, B. J., Held, I. M., Colman, R., Shell, K., and Kiehl, J. T.: Quantifying climate feedbacks using radiative kernels, *J. Climate*, 21, 3504–3520, <https://doi.org/10.1175/2007JCLI2110.1>, 2008.
- Spencer, R. W.: Global oceanic precipitation from the MSU during 1979–91 and comparisons to other climatologies, *J. Climate*, 6, 1301–1326, [https://doi.org/10.1175/1520-0442\(1993\)006%3C1301:GOPFTM%3E2.0.CO;2](https://doi.org/10.1175/1520-0442(1993)006%3C1301:GOPFTM%3E2.0.CO;2), 1993.
- Straus, D. M. and Shukla, J.: Does ENSO force the PNA?, *J. Climate*, 15, 2340–2358, [https://doi.org/10.1175/1520-0442\(2002\)015%3C2340:DEFTP%3E2.0.CO;2](https://doi.org/10.1175/1520-0442(2002)015%3C2340:DEFTP%3E2.0.CO;2), 2002.
- Subramanian, A. C., Jochum, M., Miller, A. J., Murtugudde, R., Neale, R. B. and Waliser, D. E.: The Madden Julian Oscillation in CCSM4, *J. Climate*, 24, 6261–6282. <https://doi.org/10.1175/JCLI-D-11-00031.1>, 2011.
- Tibaldi, S. and Molteni, F.: On the operational predictability of blocking, *Tellus*, 42A, 343–365, <https://doi.org/10.1034/j.1600-0870.1990.t01-2-00003.x>, 1990.
- Trenberth, K. E.: The definition of El Niño. *Bull. Am. Meteorol. Soc.*, 78, 2771–2777, [https://doi.org/10.1175/1520-0477\(1997\)078%3C2771:TDOENO%3E2.0.CO;2](https://doi.org/10.1175/1520-0477(1997)078%3C2771:TDOENO%3E2.0.CO;2), 1997.
- Trenberth, K. E., Branstator, G. W., Karoly, D., Kumar, A., Lau, N. C., and Ropelewski, C.: Progress during TOGA in understanding and modeling global teleconnections associated with tropical sea surface temperatures, *J. Geophys. Res.*, 103, 14291–14324, <https://doi.org/10.1029/97JC01444>, 1998.
- Trenberth, K. E., Fasullo, J. T., and Mackaro, J.: Atmospheric Moisture Transports from Ocean to Land and Global Energy Flows in Reanalyses, *J. Climate*, 24, 4907–4924. [10.1175/2011JCLI4171.1](https://doi.org/10.1175/2011JCLI4171.1), 2011b.
- Uppala, S. M., Kållberg, P. W., Simmons, A. J., Andrae, U., Bechtold, V. D. C., Fiorino, M., Gibson, J. K., Haseler, J., Hernandez, A., Kelly, G. A., Li, X., Onogi, K., Saarinen, S., Sokka, N., Allan, R. P., Andersson, E., Arpe, K., Balmaseda, M. A., Beljaars, A. C. M., Berg, L. V. D., Bidlot, J., Bormann, N., Caires, S., Chevallier, F., Dethof, A., Dragosavac, M., Fisher, M., Fuentes, M., Hagemann, S., Hólm, E., Hoskins, B. J., Isaksen, I., Janssen, P. A. E. M., Jenne, R., McNally, A. P., Mahfouf, J. F., Morcrette, J. J., Rayner, N. A., Saunders, R. W., Simon, P., Sterl, A., Trenberth, K. E., Untch, A., Vasiljevic, D., Viterbo, P., and Woollen, J.: The ERA-40 re-analysis, *Q. J. Roy. Meteorol. Soc.*, 131, 2961–3012, <https://doi.org/10.1256/qj.04.176>, 2005.
- Yu L. and Weller, R. A.: Objectively analyzed air-sea heat fluxes for the global ice-free oceans (1981–2005), *Bull. Amer. Meteor. Soc.*, 88, 527–539, <https://doi.org/10.1175/BAMS-88-4-527>, 2007.
- Yu, L., Jin, X., and Weller, R. A.: Multidecade Global Flux Datasets from the Objectively Analyzed Air-sea Fluxes (OAFux) Project: Latent and sensible heat fluxes, ocean evaporation, and related surface meteorological variables, Tech. Rep. OA-2008-01, Woods Hole Oceanographic Institution, Woods Hole, Massachusetts, USA, 2008.

van Vuuren, D. P., Edmonds, J., Kainuma, M., Riahi, K., Thomson, A., Hibbard, K., Hurtt, G. C., Kram, T., Krey, V., Lamarque, J.-F., Masui, T., Meinshausen, M., Nakicenovic, N., Smith, S. J., and Rose, S. K.: The representative concentration pathways: an overview. *Clim. Change*, 109, 5–31, <https://doi.org/10.1007/s10584-011-0148-z>, 2011.

Wallace, J. M., Rasmusson, E. M., Mitchell, T. P., Kousky, V. E., Sarachik, E. S., and von Storch, H.: On the structure and evolution of ENSO-related climate variability in the tropical Pacific: lessons from TOGA, *J. Geophys. Res.*, 103, 14241–14259, <https://doi.org/10.1029/97JC02905>, 1998.

Wang, Y.-M., Lean, J. L., and Sheeley, Jr., N. R.: Modeling the Sun's magnetic field and irradiance since 1713. *Astrophys. J.*, 625, 522–538, <https://doi.org/10.1086%2F429689>, 2005.

Woollings, T., Barriopedro, D., Methven, J., Son, S.-W., Martius, O., Harvey, B., Sillmann, J., Lupo, A. R., and Seneviratne, S.: Blocking and its Response to Climate Change, *Current Climate Change Reports*, 4, 287–300. <https://doi.org/10.1007/s40641-018-0108-z>, 2018.

Zhang, C.: Madden–Julian oscillation, *Rev. Geophys.*, 43, RG2003, <https://doi.org/10.1029/2004RG000158>, 2005.